 doi:10.20944/preprints201901.0078.v1

Article

NUMERICAL AND EXPERIMENTAL MODELLING OF A WAVE ENERGY CONVERTER PITCHING IN CLOSE PROXIMITY TO A FIXED STRUCTURE

Pilar Heras [1,2,*], Sarah Thomas [1], Morten Kramer [1,2] and Jens Peter Kofoed[2]

1 Floating Power Plant A/S; info@floatingpowerplant.com
2 Department of Civil Engineering, Aalborg University
* Correspondence: ph@floatingpowerplant.com; Tel.: +45 2830 7871

Version January 9, 2019 submitted to

Abstract: This paper presents a hydrodynamic numerical model for a pitching wave energy converter (WEC). The model uses potential wave theory and is based on Cummins' equation, with nonlinear hydrostatic restoring stiffness and excitation forces based on instantaneous body position and water surface elevation. The numerical model can include non-linear forces, like quadratic drag, power-take-off and other forces that may account for unknown viscous effects observed in experiments. The paper discusses the applicability and limitations of the code and presents the cases where assumptions and simplifications can be made. The goal is to conclude on the simplest, yet accurate, version of the model by evaluating its accuracy using experimental data. The case study for validation is Floating Power Plant's (FPP's) WEC [1]. In the full-scale commercial project, FPP's device consists of a semisubmersible platform hosting a wind turbine (5-8MW) and 4 WECs, each one connected to the platform by a rotation shaft. Due to the configuration of the platform, strong interactions occur between the WECs and the structure, as they are very closely spaced. In order to validate a numerical model able to simulate these hydrodynamic interactions, wave basin experiments with a similar but simplified setup were performed.

Keywords: (Wave energy, numerical model, experiments, verification, pitching)

---

1. Introduction

According to the International Energy Agency (IEA) Ocean Energy Systems (OES), wave energy technologies can be divided into three main categories: oscillating water columns, wave activated bodies, and overtopping devices. These in turn are divided into subcategories attending to the type of structure: fixed, submerged or floating. A more detailed categorization useful to make risk and failure analyses can be found in [2].

Wave developers need to prove the economic viability of their concepts and need to get funding to complete the technology development. So, despite of the large amount of wave energy concepts, none has yet been industrialised. It is essential to assess the cost models frequently and update them according to the conclusions drawn during the concept development phases. The techno-economical assessment should is as important as the evaluation of the technology readiness [3]. Wave energy developers use different software packages or codes to simulate the performance of WECs in operational and extreme conditions. Published experimental data for code validation is very limited, however some research groups, like OES Task 10 [4], are working towards the goal of building confidence in numerical estimations of loads and power production, which are key parameters in order to get a reliable and cost-efficient WEC design.

Notable interactions happen when bodies are placed close to the ocean surface with waves. In some of the practical cases, the effects of ocean waves on floating and submerged bodies can be analysed by linear potential theory. Nevertheless, this theory has not been proved to work for all types of WECs, since they may have very different specifications and configurations with different loads and interactions. Wave energy is not a mature technology, therefore there is no commercial

 doi:10.20944/preprints201901.0078.v1

software specific to compute all or the majority of the problems that can be found, the lack of published experimental data is a drawback and yet numerical models to determine the loads and motions are essential in order to bring wave and hybrid devices to commercial maturity.

There is a variety of approaches to simulate WECs, they can be grouped in three categories: linear codes, quasi-linear codes and non-linear codes. Linear codes are based on potential wave theory, computationally inexpensive and numerically stable. Quasi-linear codes (or weakly non-linear codes), consider first-order excitation and radiation forces as well, but include some non-linear effects, like instantaneous wetted surface of the body, or exact instantaneous water surface elevation given by extrapolation of the wave kinematics above the still water line. Finally, non-linear codes include boundary element models able to simulate non-linear waves and computational fluid dynamics models (CFD). Processor times of these codes are large but they are able to simulate extreme wave conditions. Quasi-linear models are computationally inexpensive compared to non-linear codes, but more expensive compared to linear ones. A comparison of codes used among different organizations working with wave energy converters simulating the same problem, consisting of a heaving sphere, can be found in [5].

A numerical model of the dynamic equation of motion for a single WEC hinged and pitching around a shaft is presented in this paper, with special focus to the WEC moving in close proximity to a fixed structure. The model solves Newton's second law, where the hydrodynamic forces on the structure include the hydrostatic restoring forces, added mass and damping from the radiation potential, incorporating free-surface memory effects, diffraction forces from incoming waves and viscous effects. The equation of motion is solved in the time domain in Matlab/Simulink with hydrodynamic parameters calculated using WAMIT, commercial software that solve the radiation and diffraction problem in frequency domain, based on linear wave theory ([6]). The time domain implementation can take extra linear and non-linear forces, i.e. quadratic drag or power-take-off forces.

Extensive experimental tests are used to validate the numerical model. Floating Power Plant is the case study, hereafter FPP. FPP's device is the result of with several years of research, wave flume, wave basin and offshore testing [7], [8]. FPP's device has 4 WECs, each one pitching around a hinge. The supporting structure for the 4 WECs is a semisubmersible moving in 6 degrees of freedom. The device is designed so that the pitching WECs interact hydrodynamically with the supporting semisubmersible structure amplifying their amplitudes of motion within the design wave frequency range. This interaction between the 4 WECs and the supporting structure has been simplified in this paper to a single wave absorber and a fixed structure located in close proximity, see Figure 1. Several configurations of the supporting structure relative to the WEC have been tested in a wave basin, as well as a range of ballast conditions of the absorber, thus providing a robust range of hydrodynamic cases. In this paper, comparison of simulation results with the experimental data is performed with a view to determining the limitations of the numerical model when applied to a pitching body in close proximity to a fixed structure and justifying assumptions or simplifications that can be made in order to obtain the most effective version of the code.

Other software packages for wave energy converters can cope with multi-body structures and closely spaced bodies, like the open-source WEC-Sim [9], or the commercial code WaveDyn developed by DNV-GL. However, the interaction between bodies that are closely located is also a modelling challenge for them, particularly pitch motion seems to be a difficult degree of freedom to model [10]. Limitations to WEC-Sim were found when trying to numerically model the experiments [11], but the identification of the code capabilities helped to plan further experimental campaigns in order to validate the software. To the author's knowledge, the validation process of these features has not been completed and/or published, hence the need of developing the numerical model presented in this paper. Once new releases of these software packages are available, code to code comparison can be performed.

 doi:10.20944/preprints201901.0078.v1

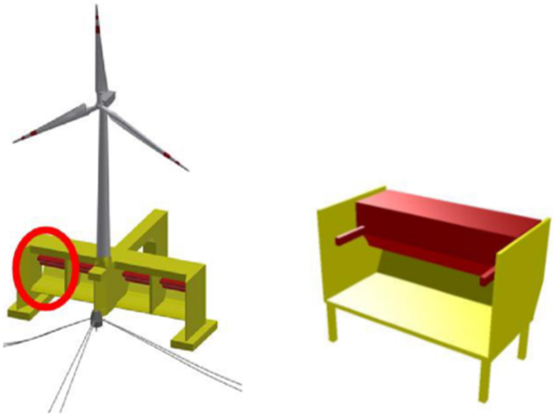

Figure 1. Left: FPP conceptual design, which counts with 4 WECs (in red). Right: Model scaled pitching wave absorber (in red), with a fixed substructure (in yellow) subject of study. Meant as simplification of the configuration highlighted in the left figure

2. Wave Basin Experiments

2.1. Laboratory setup

Testing was done in at Aalborg University, in a wave basin called "The deep 3D wave basin". The basin has the dimensions of 15.7 m long, 8.5 m wide and 1.5 m deep. Dimensions of the wave basin and location of the WEC are shown in Figure 2.

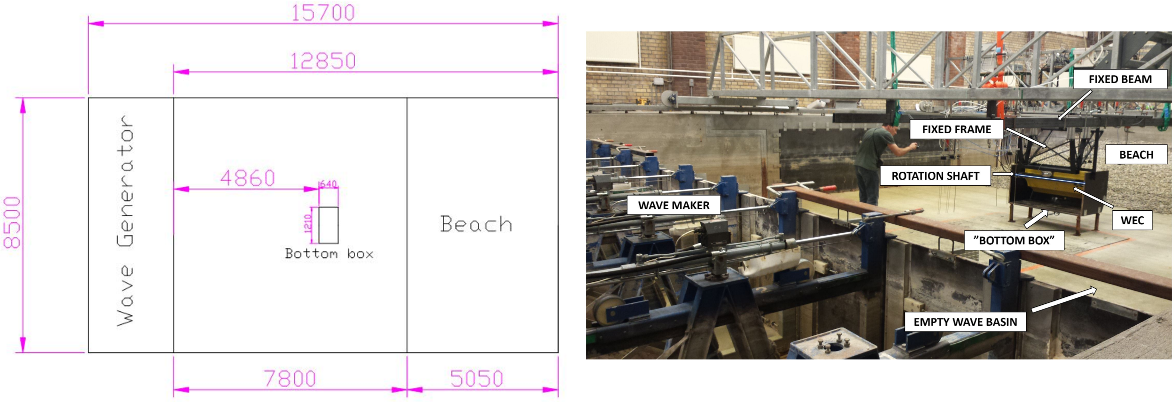

Figure 2. Left: Drawing showing position of bottom box in wave basin, bird's eye view, wave incidence 0○, measurements in mm. Right: Photo of basin with the beach in the background.

A total of 16 wave gauges were placed in the basin, see Figure 3. 12 wave gauges were placed along the centre line of the basin; 6 in front of the absorber numbered 1-6 (2 pairs of 3 gauges) and 6 behind the absorber numbered 11-16 (2 pairs of 3). The setup with the multiple wave gauges along the centre line allows for accurately separating incident and reflected waves using 2D wave analysis. The remaining 4 wave gauges numbered 7, 8, 9, 10 were placed by the side of the absorber to allow for investigation of 3D effects of diffracted and radiated waves

Preprints (www.preprints.org) | NOT PEER-REVIEWED | Posted: 9 January 2019 doi:10.20944/preprints201901.0078.v1

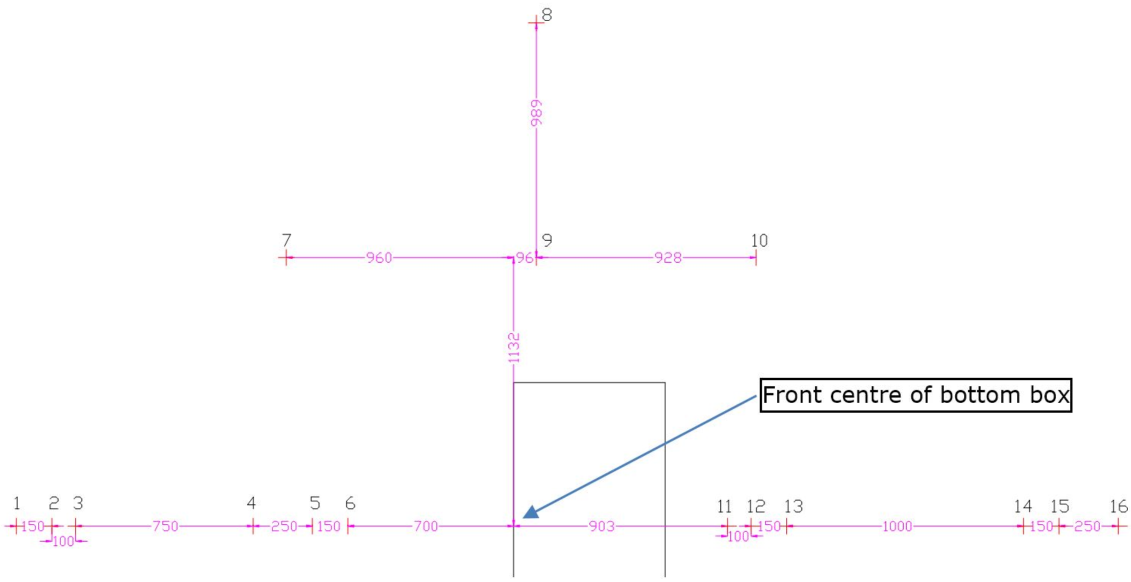

Figure 3. Position of the 16 wave gauges in the basin, plant view, measurements in mm referred to centre of front of bottom box at 0 degrees incidence position.

98 The main purpose of the wave basin tests was to investigate the influence of the surrounding fixed substructure on the performance of the WEC. Figure 4 shows the setups of the two tests used for analysis in this paper, one where the WEC is pitching with the only interaction of the waves and wave basin, and the second one where the WEC is surrounded by the fixed substructure or "bottom box" (or "BB"), which consists of two side-walls, a back wall and a bottom plate. The clearance between the inner surface of the side-walls and the outer side of the WEC is 36 mm on each side.

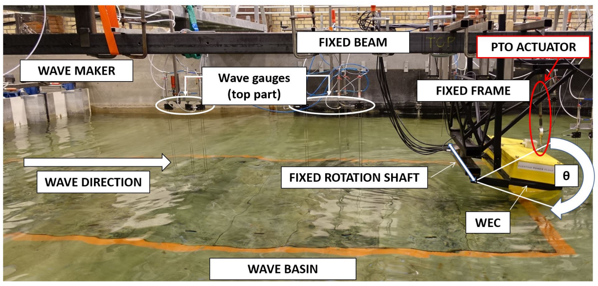

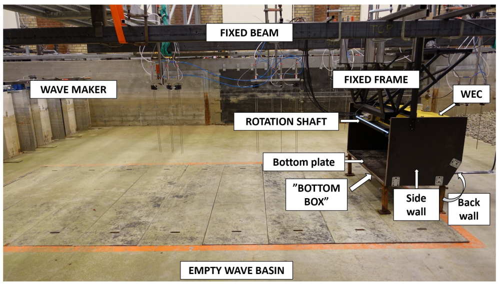

Figure 4. Left: Photo showing the in the wave basin (WEC Only). Right: Photo of the setup that consists of WEC and fixed substructure (WEC+BB). Here, the position of the WEC is the same as in the picture on the right.

2.2. Wave Basin Experimental Data

Figure 5 shows the profile of FPP's wave energy converter model used during this experimental campaign. The origin of the coordinates systems is located at the middle of the shaft going through the bearings (middle of the body), and its the axis which the body will rotate around. The moments acting on the pitching body are also shown in this figure.

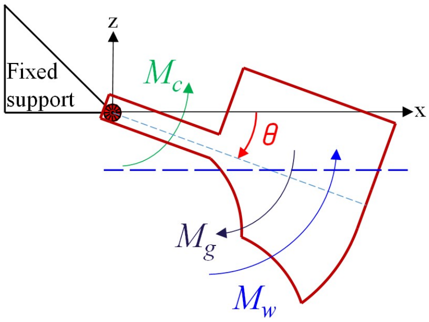

Figure 5. Pitching rigid body and moments acting on it referred to the body's origin of coordinate system. M_w is the moment from the water pressure on the body surface; M_g is the moment due to the body weigth and M_c is the moment provided by the power-take-off or control moment.

The equation governing the problem is Newton's second law:

$$J\ddot{\theta} = M_{grav} - M_w - M_c + M_{other} \tag{1}$$

Where J is the mass moment of inertia in pitch (around the y axis); $\ddot{\theta}$ is the angular acceleration of the body in pitch; M_{grav} is the gravitational moment; M_w is the moment from water pressure on the hull; M_c is the control moment from the power take off and M_{other} is the term that includes viscous and friction effects like M_{drag}, quadratic drag moment; M_{fb} friction moment from the bearings and $M_{LinearDamping}$ moment due to other viscous effects simulated in a linear way.

By inserting:

$$M_w = M_{buoy} - M_{rad} - M_{exc} \tag{2}$$

The equation is expanded to:

$$J\ddot{\theta} = M_{grav} - M_{buoy} + M_{rad} + M_{exc} - M_c + M_{other} \tag{3}$$

The experiments performed to establish the coefficients in the formulae for validation and/or calibration of the single degree of freedom model comprise:

- **Undisturbed waves and repeatability.**

  When waves are generated in the basin, some reflection effects from the beach will occur. In order to know the incident and reflected waves at the wave absorber position, the following procedure was used:
  1. Waves were generated and measured in the basin without the device (undisturbed waves) using the software "Awasys" from Aalborg University, including active absorption.

  2. A non-linear wave analysis was performed to separate incident and reflected waves using the software "WaveLab" from Aalborg University. WaveLab takes into account the propagation speed of the waves in a non-linear manner.
  3. The same waves are afterwards repeated with the device in position.

- **Free motion in regular waves.**
  In these experiments the absorber is allowed to move freely in the waves, no control moment is applied in this case.

 doi:10.20944/preprints201901.0078.v1

- **Wave excitation.**
  During these tests, the absorber was held fixed by the actuator piston. The actuator was put in position control using a fixed target position corresponding to the static, neutrally-buoyant position. The measured control moment is directly the wave excitation moment [12].

Since the absorber is held in the static position using the actuator,there is no body motion, hence Eq.3 simplifies to:

$$M_c = M_{exc} \tag{4}$$

All the experiments were performed for 16 different regular waves with periods between 0.667 and 2.5 seconds with a target wave height of 4cm. Considering the applicability of wave theories defined in [13]. In the figure, the ratio between the parameters $H_0/(gT_p^2)$ and $d/(gT_p^2)$ indicates that all the waves are non-linear, belonging to the region where the suitable wave theory is Stokes 2^{nd} order, except from the 3 shortest waves, that correspond to Stokes 3^{rd} order. Thus, stressing the objective of this paper, which is to check the suitability of a numerical method based on linear wave potential theory. The ratio between water depth d and wavelength λ, shows that the tested waves correspond to either intermediate water depth or deep water definition, and the relation between wave height and wavelength indicates the steepness of the wave. All these parameters are reflected in Figure 6.

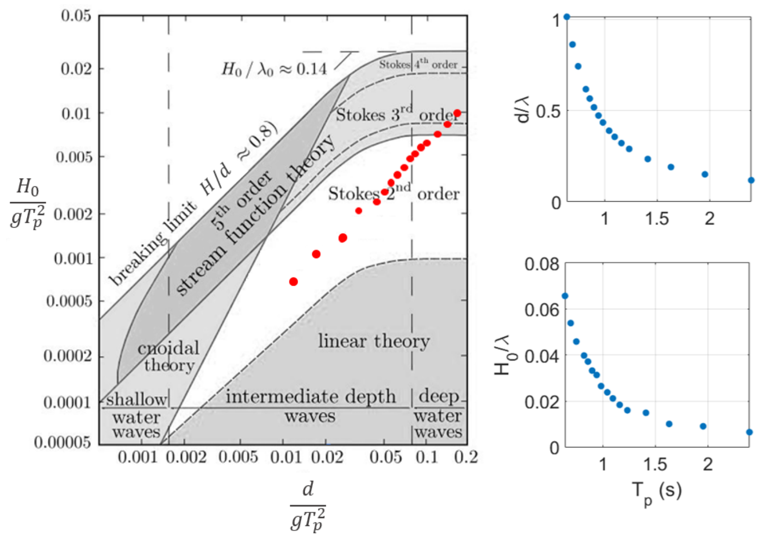

Figure 6. Left: Identification of wave theory according to the vaalidity of several theories for periodic water waves, according to Le Méhauté (1976). Right: wave steepness values corresponding to the regular wave tested. H_0 stands for wave height, $d$for water depth, g is gravity acceleration, T_p is wave period and λ is wave length.

Figure 7 illustrates the measured experimental data used. The first one includes data from the undisturbed waves experiments, the second subplot includes data from the free motion experiments in regular waves, and the third one from the wave excitation experiments.

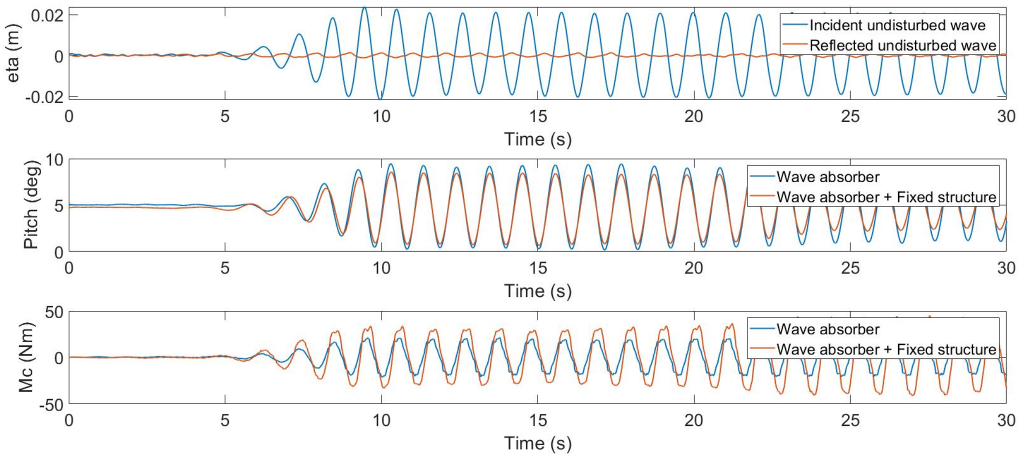

Figure 7. Wave basin experiments for $T_p = 1s$ and $H_0 = 0.04m$ regular wave. eta is wave elevation from undisturbed waves experiments; pitch the angle measured from free motion experiments, where the rest position was at 5 degrees approx., and Mc is the control moment measured during wave excitation experiments.

- **Hydrostatics**
  To measure the hydrostatic moment, the absorber was moved gently up and down and simultaneous measurements of the position and control moment were acquired as shown in Figure 8. In this case, the hydrostatic force was balanced by the control force. From these tests, the friction moment coming from the bearings can be estimated too. The friction coming from the bearings is defined by the difference of the control moment measured when moving the absorber upwards and when moving it in the opposite direction, as seen in Figure 8c, where the low curve is the moment measured when the absorber rotates downwards, and the top curve when it moves upwards. Since the signals are very irregular, the final value of the friction has been tuned within the limitations observed in these experiments in order to get a good match between the decay and free motion tests.

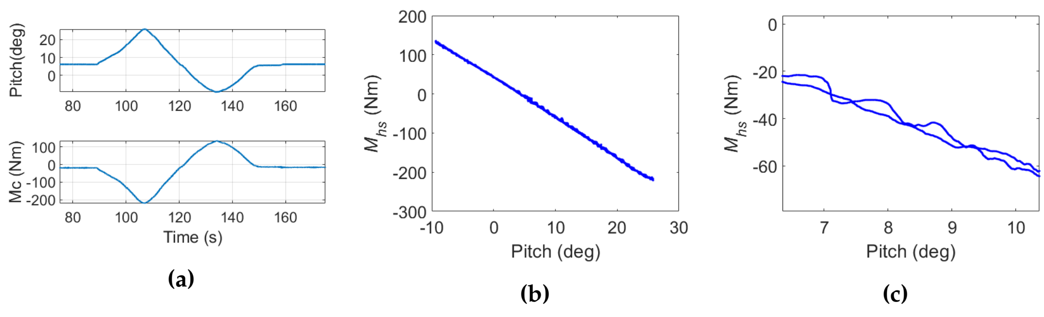

Figure 8. Hydrostatic tests. Left: Time series of hydrostatic tests. Center: Hydrostatic moment measured for a range of angles of inclinations. Right: Zoom in of the hydrostatic moment measured for a range of inclinations.

- **Decay**
  An example of a (repeated) decay test is shown in Figure 9a. In the decay tests, the WEC was lifted (or pushed down) using the actuator, which was set to provide a constant moment in order to keep the WEC away from its static position for a few seconds before releasing it. As illustrated,

when repeating the decay tests for the same conditions, very similar motions are observed. The difference between target and measured moment provided by the actuator is presented in Figure 9b, where the irregularities in the measured moment are due to friction effects.

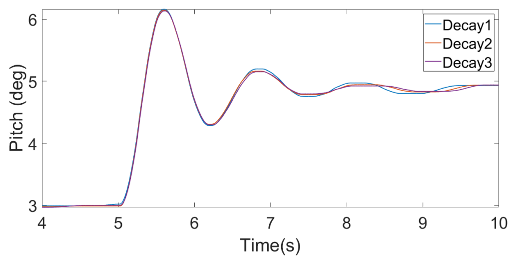

(a) Decay tests with absorber released at t=5s for the setup of WEC only.

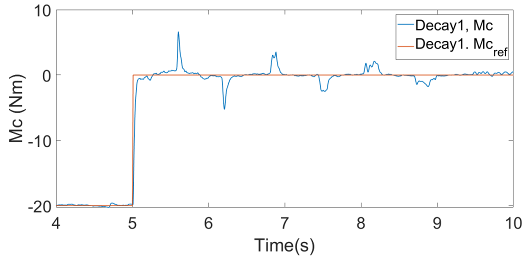

(b) Target and measured control moment corresponding to the first decay test.

Figure 9. Example of data for decay tests for the case of WEC only, Figure 9a shows the repeatability of the experiment, and Figure 9b shows the difference between target and measured control moment.

After an analysis of the undisturbed wave experiments, some conclusions can be drawn. It is very important to simulate the same wave conditions with the numerical model, since the motion of the absorber will rely on the incoming wave. A common quantity to analyse the performance of a floating body is the Response Amplitude Operator (RAO), that represents the ratio between the motion amplitude relative to the wave amplitude. The RAO will be calculated with the peaks and troughs of the sinusoidal motion and peaks and troughs of the sinusoidal wave. The number of peaks has been chosen by selecting some of the fully developed waves that are less affected by reflection, meaning the first waves after reaching 90% of the target wave height. Figure 10 displays an example of a time series and the peaks to choose among to define the response amplitude operator. As reflections of waves hits the absorber early in the signal it is important to choose the time for analysis wisely. It is chosen to show examples of this selection with the shortest and longest regular wave period

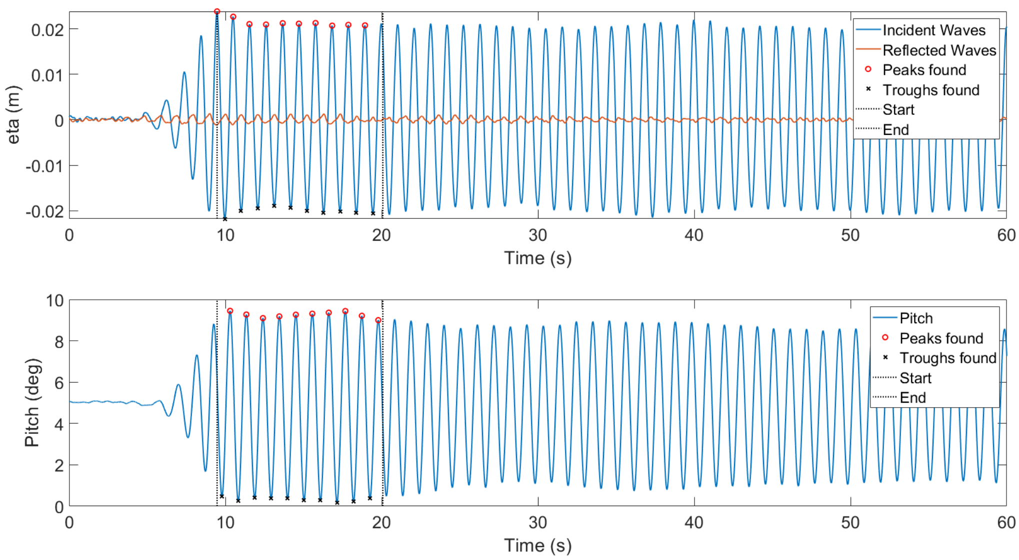

Figure 10. Example of time series of undisturbed wave experiments and the corresponding free floating experiment. The vertical lines define the time window where peaks and troughs are found and can be used to calculate the RAO.

Depending on the number of waves included in the analysis, the RAO curve may vary. Figures 11 and 12 illustrate how this parameter changes depending on the number of waves used on the calculation.

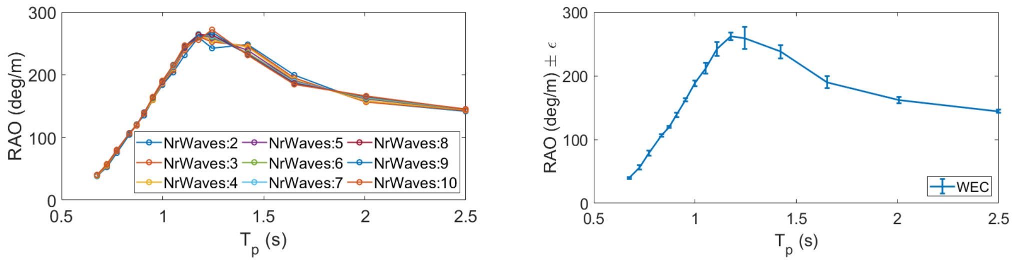

Figure 11. Left: RAO calculated for different number of waves for the setup of WEC only. Right: RAO showing the error caused by the number of waves chosen.

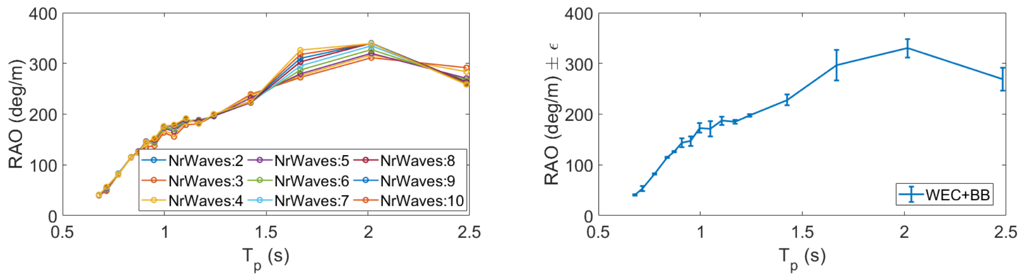

Figure 12. Left: RAO calculated for different number of waves for the setup of WEC+BB. Right: RAO showing the error caused by the number of waves chosen.

3. Model description

The numerical model baseline is a set of data of hydrodynamic coefficients calculated using WAMIT for a range of frequencies and for different body positions, which are defined by the angle of inclination of the WEC. The hydrodynamic quantities corresponding to the pitch degree of freedom for the hydrostatic rest position of the body for different wave periods are shown in Figure 13. A deeper analysis on the hydrodynamic coefficients calculated by WAMIT used in a linear numerical model was performed in [14].

Preprints (www.preprints.org) | NOT PEER-REVIEWED | Posted: 9 January 2019 doi:10.20944/preprints201901.0078.v1

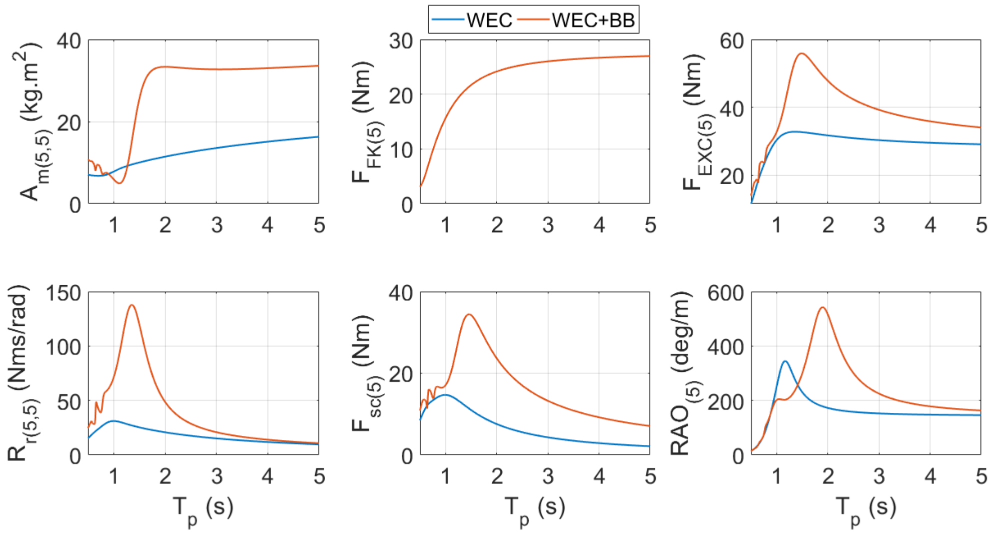

Figure 13. Hydrodynamic quantities evaluated using WAMIT. Being A_m, added mass; R_r, radiation damping; F_{FK}, Froude-Krylov force modulus; F_{SC}, scattered force modulus; F_{EXC}, excitation force modulus and RAO the response amplitude operator.

It is important to highlight that despite of the overestimation of the pitch motion by linear theory, linear theory is able to predict the overall interactions between the two bodies, as Figure 14 reflects. As the figure shows, the inclusion of the surrounding body alters the performance of the WEC for a range of wave frequencies . However, this influence is not positive for waves with period between 1 and 1.4 seconds. Thus, the importance of understanding and being able to simulate the multi-body interactions, in order to modify the physical setup in order to optimize WEC performance for the desired range of wave periods and so, power production.

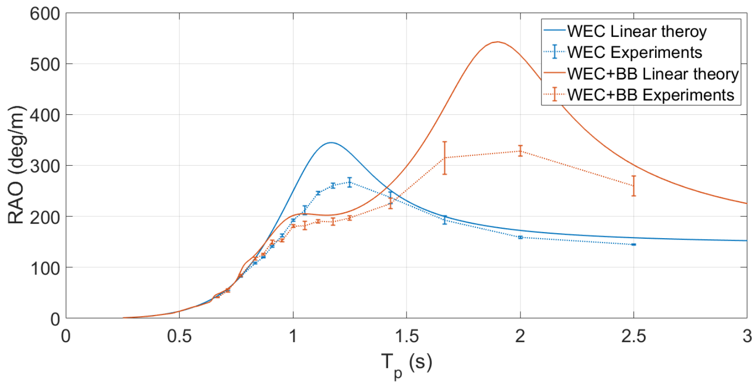

Figure 14. Response Amplitude Operators calculated using linear theory (solid lines) and experimental data (dashed lines). Experimental results include the error of the parameters as in Figure 11 and 12. Both results show that the inclusion of the fixed structure around the WEC modify the behaviour of the WEC, decreasing its motion for wave periods up to 1.4 s and increasing it for the longest waves.

Eight numerical model versions are compared. In order to make it easier to understand the calculation methods used in each of the stages, a table is included in Tables 1. The version 1 of the model, $V1$, corresponds to the linear numerical model. In the table, $\eta_{REG}(t)$ stands for a theoretical regular wave, $\eta_{EXP}(t)$ stands for experimental measurements of a target regular wave. The rest of the parameters are explained later in this section.

 doi:10.20944/preprints201901.0078.v1

Linear theory considers that the water surface elevation is equal to zero, which is represented by the still water line (SWL) in the figures. Displacement is used to analyse the motion of the wave energy absorber, and it is defined as the amplitude of its motion (angle rotated relative to rest position).

Table 1. Numerical model versions description

Forces	**V1**	**V2**	**V3**	**V4**	**V5**	**V6**	**V7**	**V8**
eta	$\eta_{REG}(t)$	$\eta_{REG}(t)$	$\eta_{REG}(t)$	$\eta_{REG}(t)$	$\eta_{REG}(t)$	$\eta_{EXP}(t)$	$\eta_{EXP}(t)$	$\eta_{EXP}(t)$
$J + A_m$	θ_0	θ_0	θ_0	θ_0	θ_0	θ_0	θ_0	θ_0
M_{rad}	θ_0	θ_0	θ_0	θ_0	θ_0	θ_0	θ_0	θ_0
M_{grav}	θ_0	θ_i	θ_i	θ_i	θ_i	θ_i	θ_0	θ_i
M_{buoy}	θ_0	θ_i	θ_i	θ_i	θ_i	θ_i	θ_0	θ_i
M_{FK}	θ_0	θ_i	$\tilde{\theta}_0$	$\tilde{\theta}_0$	$\tilde{\theta}_0$	M_{exc}^{IRF}	M_{exc}^{IRF}	M_{exc}^{IRF}
M_{sc}	θ_0	θ_i	θ_i	θ_i	θ_i			
$M_{drag}: \quad C_d$	0	0	0	2	2	2	2	2
M_{fb}	0	0	0	0	0	0	0.4	0.4
$M_{LinearDamping}$	0	0	0	0	0	0	0	$-B\dot{\theta}$

The inclusion of a control moment M_c applied by the actuator only occurs for the decay simulations and the input to the model is the measured signal.

The model solves the dynamic equation of motion defined in Eq.3. The moments can be grouped or decomposed as:

$$M_{hyst} = M_{grav} + M_{buoy}$$

$$M_{exc} = M_{FK} + M_{SC}$$

$$M_{losses} = M_{drag} + M_{fb} + M_{LinearDamping}$$

Where, M_{hyst} is the hydrostatic stiffness moment;M_{grav}, the gravity moment; M_{buoy}, the buoyancy moment; M_{exc} the excitation moment; M_{FK}, Froude-Krylov moment; M_{sc}, scattered moment; M_{drag}, quadratic drag moment; $M_{FrictionBearing}$, the moment due to the friction in the bearings and $M_{LinearDamping}$ a moment due to linear damping.

The submerged body is defined by its submerged panel centroids. The panel centroids and their normals are defined for an angle of the body equal to zero according to the body coordinates system given in Figure 15, and then rotated as needed using the following rotation matrix [15]

$$R_y(\theta) = \begin{bmatrix} cos(\theta) & 0 & sin(\theta) \\ 0 & 1 & 0 \\ -sin(\theta) & 0 & cos(\theta) \end{bmatrix} \tag{5}$$

Withe the aim of speeding up all of the calculations that use panel centroids, only a portion or slice in the y direction of the WEC is used. To scale volume and loads to the actual size of the body, a width ratio is apply afterwards. Figure 15 presents a top view of half of the WEC in blue, and in red the slice of the absorber used to make the method more efficient. This simplification can be made because, even though the hinge arms can get slightly submerged, that doesn't change significantly the total submerged volume or the geometry that defines the hydrodynamic coefficients.

 doi:10.20944/preprints201901.0078.v1

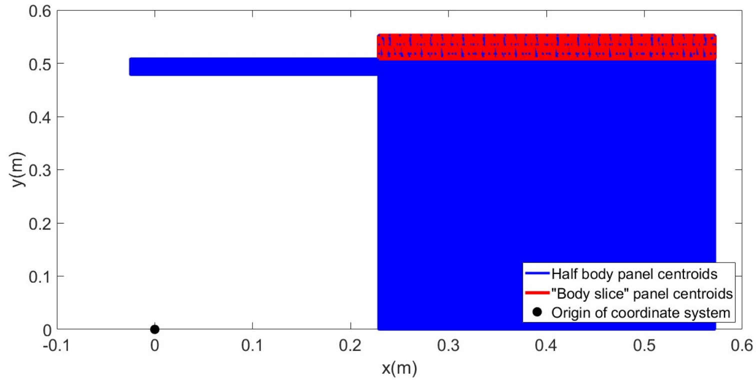

Figure 15. Top view of panel centroids of (half) body and selected slice.

- **Radiation moment:** M_{rad}
  The radiation moment has been included as a memory function approximated using Prony's method in the time domain model [16]. This moment is calculated using the coefficients for the absorber's rest position.

$$M_{rad} = -A_{\infty}\ddot{\theta}(t) - \int_0^t K(t-\tau)\dot{\theta}(\tau)d\tau \tag{6}$$

  Where A_{∞} is the infinite frequency added mass and $\ddot{\theta}$ is the pitch acceleration, this term represents the contribution to the force that is in phase with the body acceleration. $\int_0^t K(t-\tau)\dot{\theta}(\tau)d\tau$ is the convolution term that accounts for the fluid memory effects, where K is the retardation function, which can be calculated in the time domain using the damping coefficients.

$$K(t) = \int_0^{\infty} B(\omega)cos(\omega t)d\omega \tag{7}$$

- **Hydrostatic moments:** $\mathbf{M_{hyst}}$
  The hydrostatic moment is due to the difference between the torque due to the body mass or gravity torque, and the buoyancy torque.
  - **Gravity moment:** $\mathbf{M_{grav}}$
    The gravity torque depends on the body position defined by the angle of rotation θ. The torque will be estimated at the rest position (θ_0) when using linear theory and at the instantaneous body position, θ_i, when using the quasi-linear numerical model.

$$M_{grav(5)}(\theta) = JgCOB_x(\theta) \tag{8}$$

    Where J is the $(5,5)$ element of the inertia matrix, which is the moment of inertia of the body around the y axis, and COB_x is the x coordinate of the center of buoyancy.
  - **Buoyancy moment:** $\mathbf{M_{buoy}}$
    * In general terms, the linear hydrostatic stiffness moment M_{hyst} is a linearization of the difference between the buoyancy and gravity moments, assuming small amplitudes of motion, hence, small changes in waterplane area, such that:

$$M_{hyst(5)} = -K_{(5,5)}X_5 \tag{9}$$

Preprints (www.preprints.org) | NOT PEER-REVIEWED | Posted: 9 January 2019 doi:10.20944/preprints201901.0078.v1

Where $K_{(5,5)}$ is the $(5,5)$ component of the linear hydrostatic stiffness coefficient matrix and X_5 is the body's displacement in the 5^{th} degree of freedom.
In the current numerical model, stiffness moment is split in the equation of motion into the separate gravity and buoyancy components, hence the linear stiffness is replaced such that:

$$M_{hyst(5)} = M_{grav(5)} + M_{buoy(5)} = -K_{(5,5)}X_5 \tag{10}$$

$M_{grav(5)}$ can be calculated as above, and for the case where the linear stiffness coefficient is to be used, $M_{buoy(5)}$ is calculated from:

$$M_{buoy(5)} = -K_{(5,5)}X_i - M_{grav(5)} \tag{11}$$

The hydrostatic coefficient $K_{(5,5)}$ is obtained from WAMIT for the rest position θ_0.

* The buoyancy force can also be calculated by integrating the static pressure across the instantaneous submerged body geometry defined by the angle of rotation θ_i, where the instantaneous submerged geometry is divided into n panels. Panel $j \in (1:n)$ has a centroid with coordinates $c_j = [c_1, c_2, c_3]_j$ and normal $n_j = [n_1, n_2, n_3]_j$ in the x, y and z directions respectively, and surface area S_j.
The surge, sway and heave buoyancy forces are first given by:

$$F_{buoy(i)}(\theta_i) = -\rho g \sum_{j=1}^{n} (c_3(\theta_i) S n_i)_j \quad for \quad i \in [1:3] \tag{12}$$

Then, based on these, the rotational modes roll, pitch and yaw are given by:

$$M_{buoy(i)}(\theta_i) = [c_1, c_2, c_3] \times [F_{buoy(1)}, F_{buoy(2)}, F_{buoy(3)}] for \quad i \in [4:6] \tag{13}$$

Where $\times$ represents cross product.
Therefore, for a pitching device the buoyancy force is given by:

$$M_{buoy(5)} = c_3 F_{buoy(1)} - c_1 F_{buoy(3)} \tag{14}$$

- **Excitation moment: $\mathbf{M_{exc}}$**

  - **Froude-Krylov moment: $\mathbf{M_{FK}}$**
    Froude-Krylov forces are based on the formulation of the dynamic pressure according to linear theory:

$$p_D = \rho g \frac{H}{2} \frac{\cosh\left(k\left(z+d\right)\right)}{\cosh(kd)} \cos(kx - \omega t) \tag{15}$$

Where, ρ is water density; g, gravity acceleration; H, wave height; k, wave number; d, water depth; ω, wave frequency; t is the time and z and x are vertical and horizontal coordinates, respectively. The three possible approaches included in the numerical model are:

* **Regular sinusoidal propagating waves and body rest position**
Corresponding to the linear formulation. The Froude-Krylov moment is determined by integrating the dynamic pressure across the submerged geometry at the hydrostatic rest position (θ_0), where the submerged geometry is defined by the still water line.

$$F_{FK(i)}(\theta_0) = \rho g \frac{H}{2} \sum_{j=1}^{n} \left(\frac{\cosh\left(k\left(c_3(\theta_0)+d\right)\right)}{\cosh(kd)} \cos(kc_1(\theta_0) - \omega t) S(\theta_0) n_i(\theta_0) \right)_j, \quad i \in [1:3] \tag{16}$$

Preprints (www.preprints.org) | NOT PEER-REVIEWED | Posted: 9 January 2019 doi:10.20944/preprints201901.0078.v1

Where, in addition to the parameters using to define the dynamic pressure, this equation also uses the panel centroid coordinates c_i, the submerged surface area S and the normal vectors to the panels n.

* **Regular sinusoidal propagating waves and instantaneous body position**
Determined by integrating the dynamic pressure across the instantaneous submerged geometry, where the instantaneous submerged geometry is defined by the still water line.

$$F_{FK(i)}(\theta_i) = \rho g \frac{H}{2} \sum_{j=1}^{n} \left(\frac{\cosh\left(k\left(c_3 + d\right)\right)}{\cosh(kd)} \cos(kc_1 - \omega t) S n_i \right)_j, \quad i \in [1:3] \tag{17}$$

* **Regular waves and instantaneous body position with Wheeler stretching**
Determined by integrating the dynamic pressure across the instantaneous submerged geometry, where the instantaneous submerged geometry is defined by the submerged panels according to the instantaneous water surface with Wheeler stretching implemented as in [17]. The surge, sway and heave Froude-Krylov forces are first given by:

$$F_{FK(i)}(\tilde{\theta})_i = \rho g \frac{H}{2} \sum_{j=1}^{n} \left(\frac{\cosh\left(k\left(\frac{c_3 - \eta}{1 + \frac{\eta}{d}} + d\right)\right)}{\cosh(kd)} \cos(kc_1 - \omega t) S n_i \right)_j, i \in [1:3] \tag{18}$$

In this case, η is the water surface elevation at the x coordinate c_1 at time t.

Then, based on the Froude-Krylov forces, the rotational modes roll, pitch and yaw are given by:

$$M_{FK(i)} = [c_1, c_2, c_3] \times [F_{FK(1)}, F_{FK(2)}, F_{FK(3)}], \quad i \in [4:6] \tag{19}$$

– **Scattering moment: $\mathbf{M_{sc}}$**
The scattering force can be determined by:

* With WAMIT scattered moment coefficients corresponding to the absorber's rest angle.

$$M_{sc(5)}(\theta_0) = |M_{sc(5)}(\theta_0)| \frac{H}{2} \cos(\omega t + \varphi_{sc(5)}(\theta_0)) \tag{20}$$

* Interpolating different WAMIT scattered moment coefficients corresponding to different angles of absorber to update this moment each time-step to the actual absorber angle of inclination.

$$M_{sc(5)}(\theta_i) = |M_{sc(5)}(\theta_i)| \frac{H}{2} \cos(\omega t + \varphi_{sc(5)}(\theta_i)) \tag{21}$$

– **Excitation moment: $\mathbf{M_{exc}(t)}$**
The excitation torque can be calculated by convolving the water surface elevation with the impulse response function of the linear excitation torque, as shown in Eq. 22, where $\eta(t)$ is the undisturbed measured wave time series[18].

$$M_{exc}(t) = M_{exc}^{IRF}(t)\eta(t) = \int_{-\infty}^{\infty} M_{exc}^{IRF}(t-\tau)\eta(\tau)d\tau \tag{22}$$

The impulse response function of the excitation moment, M_{exc}^{IRF}, is calculated by taking the inverse Fourier transform of the frequency response, as in Eq.23.

$$M_{exc}^{IRF}(t) = \frac{1}{2\pi} \int_{-\infty}^{\infty} M_{exc}(\omega) e^{i\omega t} d\omega \tag{23}$$

$M_{exc}(\omega)$ is the linear excitation force defined by its module and phase, which are calculated computing WAMIT for the hydrostatic rest position of the WEC. The calculated excitation force is an exogenous input to the hydrodynamic numerical model, as it does not depend on the body motion.

- **Quadratic drag moment:** $\mathbf{M_{drag}}$
The quadratic drag model is based on Morison formulation and uses the relative velocity between the WEC and the fluid. It uses a mesh-approach based on panels that define the geometry of the absorber, as for calculate Froude-Krylov or buoyancy moments. Two methods to calculate the quadratic load can be used: the first one is the the exact method, that computes the quadratic loading at each panel by calculating the relative velocity between the panel and the fluid velocity at its centroid at each time-step. The second is an approximated quadratic load, that approximates the entire submerged geometry by a single flat surface and computes the quadratic load using the relative velocity between this panel and the fluid velocity at its centroid, at each time-step.

1. A quadratic drag force in the translational modes can be implemented as follows,

$$F_{drag(i)} = -\sum_{j=1}^{n} \frac{1}{2} \rho C_d A_{p(i,j)} (\dot{X}_{(i,j)} - u_{(i,j)}) |\dot{X}_{(i,j)} - u_{(i,j)}|, \quad i \in [1:3] \tag{24}$$

Where C_d is the drag coefficient, $A_{p_{(i,j)}}$ is the projected area of the j panel in the i direction, $\dot{X}_{(i,j)}$ the j panel velocity in the i direction and $u_{(i,j)}$ the fluid velocity at the j panel centroid in the i direction. n is the total number of submerged panels. Further details can be found in [19].

The implementation of the quadratic drag force has been as follows:

1. Definition of the submerged body position at each time-step and at the previous one. The body position is calculated by multiplying the panel centroid coordinates by the rotation matrix in Eq. 5 define for the angle of rotation. Only the panels below the instantaneous water surface elevation are taken into account.

2. Definition of the body velocity based on the change in position of the panel centroids coordinates each time-step:

$$\dot{X} = \frac{X(t_i) - X(t_{i-1})}{t_i - t_{i-1}} \tag{25}$$

$X = [c1, c2, c3]$ indicates the coordinates of the panel centroids. Since we are using the panels coordinates in the body coordinate system to calculate the body velocity, as result the velocity obtained is $\dot{X} = (\dot{x}, \dot{y}, \dot{z})$, referring to the (x, y, z) components. This is needed to calculate later on the relative velocity between the body and the fluid.

3. Calculate the projected area of the panels below the water surface.
The geometry is defined by panels, which are defined by four vertices. Three-dimensional panel surfaces defined by four vertices can be estimated by dividing them into two triangles and calculating the area of each of them as follows [20]:

$$A = \frac{1}{2} |(\mathbf{x}_2 - \mathbf{x}_1) \times (\mathbf{x}_1 - \mathbf{x}_3)| \tag{26}$$

Preprints (www.preprints.org) | NOT PEER-REVIEWED | Posted: 9 January 2019 doi:10.20944/preprints201901.0078.v1

Where $\mathbf{x}$ represents a vertex defined by three coordinates, $\mathbf{x} = [x_1, x_2, x_3]$ and $\times$ is the cross product.
In order to calculate the projected area of a triangle in the x, y and z directions, this equation is used:

$$Ap_x = \frac{1}{2}|(\mathbf{x}_{2x} - \mathbf{x}_{1x}) \times (\mathbf{x}_{1x} - \mathbf{x}_{3x})| \tag{27}$$

Where, $\mathbf{x}_{nx} = [0, x_2, x_3]$, and here n is the vertex number. Analogously, the vertex defining the projected area in the y direction will have the y component equal to 0, and will keep the x and z coordinate components. In the same way, in order to calculate Ap_z all the z coordinates of the vertex will be set to 0, and only the x and y coordinate components will be used in the calculation.
4. Calculate the fluid velocity and relative velocity.

In linear theory, the velocity potential is related to the complex velocity potential by:

$$\Phi = Re(\varphi e^{i\omega t}) \tag{28}$$

Where the complex velocity potential is defined by:

$$\varphi_0 = \frac{igH}{2\omega}\frac{cosh(k(z+d))}{cosh(z+d)}e^{-ikx\cos\beta - ikx\sin\beta} \tag{29}$$

Where k is the wavenumber and β is the angle between the positive x-axis and the direction of propagation of the incident wave.
For $\beta = 0$, the fluid velocity in the y direction $u_y = 0$, and the horizontal and vertical velocities are given by:

$$u_x = Re\left(\frac{H}{2}\frac{gk}{\omega}\frac{cosh(k(z+d))}{cosh(z+d)}e^{-i(kx-\omega t)}\right) \tag{30}$$

$$u_z = Re\left(i\frac{H}{2}\frac{gk}{\omega}\frac{sinh(k(z+d))}{cosh(z+d)}e^{-i(kx-\omega t)}\right) \tag{31}$$

Hence, the pitching relative velocity between the wave absorber and the fluid is:

$$(\dot{X} - u) = [\dot{x} - u_x, 0, \dot{z} - u_z] \tag{32}$$

5. By observing how the panel normal and panel velocity vectors change in time domain, it was concluded that the condition for the panels to meet in order to contribute to the drag force is that the angle defined by the panel normal vector and the panel velocity vector is less than 90 degrees. This condition will define which panels will contribute to the drag force when the device is moving downwards or clockwise, and which panels will contribute when the device is rotating upwards.
This angle is calculated using the cross product and the dot product as follows [21]:

$$beta = arctan\frac{||\mathbf{n}_p \times \dot{\mathbf{X}}||}{\mathbf{n}_p \cdot \dot{\mathbf{X}}} \tag{33}$$

6. The drag force in (x, y, z) can now be calculated using Eq.24, and the corresponding moments will be given by:

$$M_{drag(i)} = \sum_{j=1}^{n}[c_1, c_2, c_3]_j \times [F_{drag(1)}, F_{drag(2)}, F_{drag(3)}]_j, \quad i \in [4:6] \tag{34}$$

Preprints (www.preprints.org) | NOT PEER-REVIEWED | Posted: 9 January 2019 doi:10.20944/preprints201901.0078.v1

2. An approximate quadratic drag can be implemented in order to simplify and speed up calculations. This quadratic drag force is calculated for a hypothetical one single flat panel which would substitute all of the panels defining the submerged panels taken into account when calculating drag in the previous way. The flat panel that is used to calculate this approximated force is illustrated in Figure 16. In this case the equation of the quadratic drag force is simplified as follows:

$$F_{drag(i)} = -\frac{1}{2}\rho C_d A_{p,i} \dot{X}_i |\dot{X}_i|, \quad i \in [1:3] \tag{35}$$

With the moments corresponding to these forces defined by:

$$M_{drag(i)} = [c_1, c_2, c_3] \times [F_{drag(1)}, F_{drag(2)}, F_{drag(3)}], \quad i \in [4:6] \tag{36}$$

Here again, $\dot{X}_i$ represents translational body velocity in the x, y and z directions and $A_{p,i}$ is the projected area of the flat panel and $c1, c2, c3$ are the coordinates of the centroid of this panel, which is shown in Figure 16. This force is only computed when the absorber is pitching clockwise.

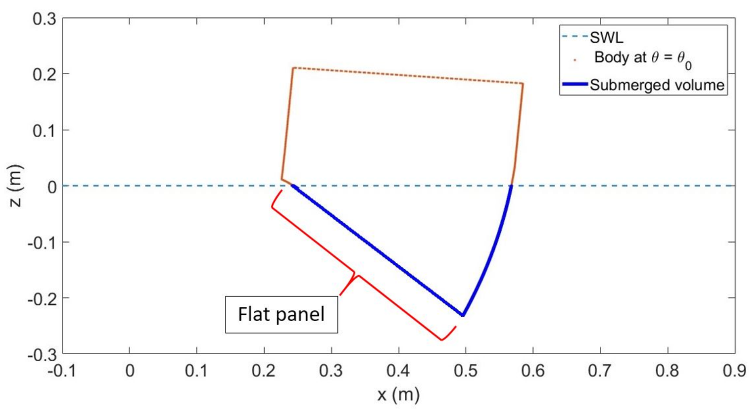

Figure 16. Geometry used to calculate an approximation of the quadratic drag force.

This diagonal flat panel has very similar projected area in the x and z direction as the one resulting from the sum of all the panel areas for the actual body geometry used for the exact formulation. Hence the quadratic force obtained is equivalent, however the computational time will be reduced significantly.

The first option, or exact formulation, is computationally more expensive, since the submerged volume of the slice of the WEC is define by a large number of panels (2000, approx.). Each time-step the submerged panels, panels velocities and fluid velocities at the centroids has to be calculated; whereas in the approximated approach, only one relative velocity has to be calculated since the surface contributing to the quadratic drag moment has been approximated by one flat panel. Although in the approximate approach, the submerged "boundary" panels that will define the area of the panel are still computed at each time-step too.

- **Friction in the bearings:** $\mathbf{M_{fb}}$
  The value of the friction in bearing has been estimated from hydrostatics tests. The friction moment has been implemented as a constant moment against the WEC's motion:

$$M_{fb} = K sign(\dot{\theta}) \tag{37}$$

 doi:10.20944/preprints201901.0078.v1

- **Linear Damping:** $\mathbf{M_{LinDamp}}$
  The unknown effects that cause the body motion to be damped are included as a linear damping moment $M_{LinDamp}$. The linear damping coefficient B will be chosen based on experimental data.

$$M_{LinDamp} = -B\dot{\theta} \tag{38}$$

4. Results

In this section, some simulations are compared with experimental data in order to draw conclusions about the numerical model. The hydrodynamic numerical model is based on potential theory, but can include nonlinear hydrostatic restoring stiffness and Froude-Krylov based on pressure integration in the instantaneous wetted surface defined by the wave elevation, instantaneous scattered forces, quadratic drag forces and other friction forces, such as friction from the bearings and linear damping. Figure 17 presents a comparison between all the model stages defined before. The influence of the instantaneous body position is small compared with the effect of the quadratic drag force.

In Figure 17 a comparison of the different versions of the model is made by comparing the RAO of their simulations. Figure 17a compares versions 1 to 5. V1 is linear theory, whose results are greater than those from V2, which computes non linear hydrostatic stiffness and Froud-Krylov torque. V3 extrapolates the wave kinematics above the water surface using Wheeler stretching when integrating pressures, but this feature doesn't add major changes and results from V2 and V3 look the same. V4 is built up from V3, and includes the exact formulation of quadratic drag loading, which reduces the motion significantly compared to V3, but stays the same as V5, which approximates the quadratic drag forces.

Figure 17b presents results from the versions that include quadratic drag, plus linear theory results. The values of the quadratic drag coefficients are based on values found in literature for other geometries [22]. CFD analysis would be needed to find a more correct value of this parameter. The difference between V5 and V6, is that the excitation forces are numerically calculated in V5, and calculated from the measured wave data from the undisturbed waves experiments in V6. V7 and V8 include bearings friction, which didn't apply in V6. V7 considers linear stiffness, whereas V8 computes the stiffness for the instantaneous body position. Since V8 has non-linear stiffness, and include quadratic drag and friction effects, is considered to be the more realistic version of the numerical model and is the one chosen to perform the numerical simulations.

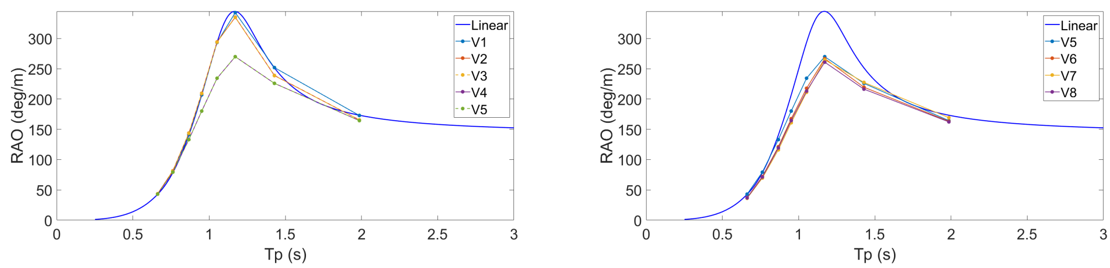

(a) Numerical model versions 1 to 5 compared to linear theory

(b) Numerical model versions 5 to 8 compared to linear theory

Figure 17. Numerical model versions analysis by comparison of RAOs

Results from V4 and V5 (see Table 1) are included in Figure 18 to prove that the simplification of the quadratic drag is acceptable. The difference of the calculated drag moment is shown in the third plot of Figure 18. It can be observed that both methods show good agreement when the floater is pitching downwards. However, when it is rotating upwards, the approximated version doesn't compute any load, but the value of the mesh-based calculated drag load when the absorber is rotated upwards, is relatively small and happens for a short period of time. Hence, it is fair to approximate the drag moment by a simplified submerged geometry. V5 is more optimal since is computationally less expensive (approximately 4 times faster).

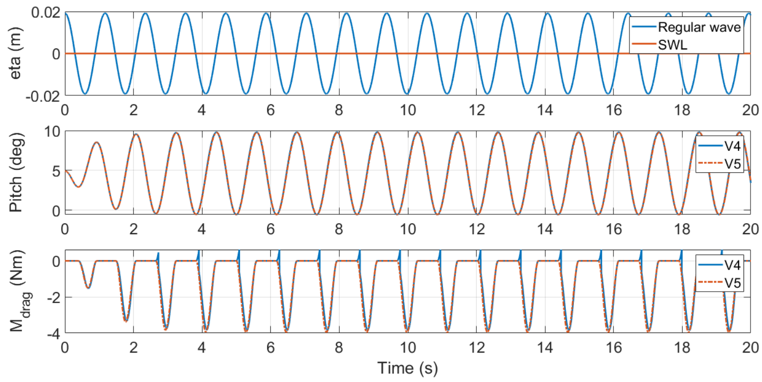

Figure 18. Comparison of exact and approximated formulation of quadratic drag. In the figure, *eta* is the water surface elevation, and M_{drag} is the moment around the y axis corresponding to the quadratic drag forces in the x and z directions.

4.1. Decay tests simulations

In the decay tests the WEC was moved from its static equilibrium by using the actuator, which held it for a few seconds either up or down from the rest position, which is approximately at 5 degrees. When the WEC was released, it came back to the static equilibrium after very few oscillations. The oscillations are damped out quickly due to radiated waves, so the potential energy dissipated with the wave radiation.

Figure 19 shows how sensitive the numerical model is to the physical inputs. Two of the parameters that affect the results the most are water depth and friction coming from the bearings. Both of them are very difficult to determine with exact precision. Figure 19a shows how 1 mm of difference in water depth affects the simulated performance of the absorber. The accuracy in the manual measurements and the differences due to changes in water depth are estimated to be +/- 1mm. This does not sound like much, but as the hinge height, which is the origin of the coordinates system, was fixed relative to the seabed with a target height of 50 mm above the still water surface, 1 mm actually corresponds to an accuracy in this hinge height of +/- 2%. This accuracy corresponds to a change in rest angle of about ± 0.15 degrees and impacts the hydrodynamics.

Figure 19b presents how the friction in the bearing where the WEC is rotating around influences the results. From the hydrostatics test presented before, the friction from the bearings was estimated to be less than 1Nm.

Preprints (www.preprints.org) | NOT PEER-REVIEWED | Posted: 9 January 2019 doi:10.20944/preprints201901.0078.v1

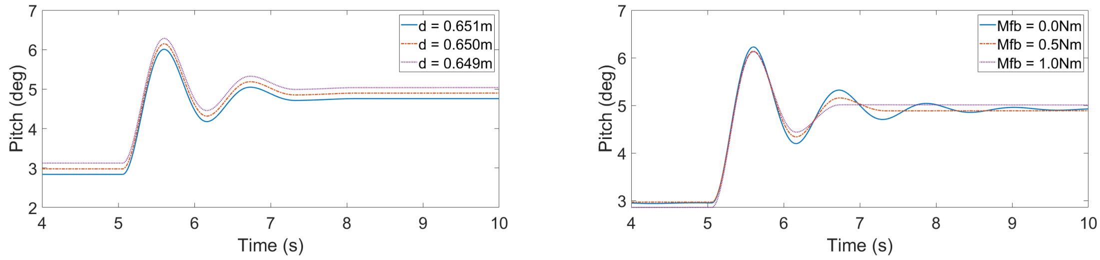

(a) Influence of 1mm difference in water depth, d, on the calculated absorber position during a decay test.

(b) Influence of the moment due to friction in the bearings, M_{fb}, on the calculated absorber motion during a decay test.

Figure 19. Importance of experimental inputs in decay test simulations

As stated, the numerical model is very sensitive to the inputs, even though the experimental inputs have been defined with the highest level of accuracy possible. Therefore, some assumptions need to be made. The values of quadratic drag coefficient and friction from bearings have been estimated by calibrating the numerical model to fit the experimental data are $C_d = 2$ and $M_{fb} = 0.4Nm$.

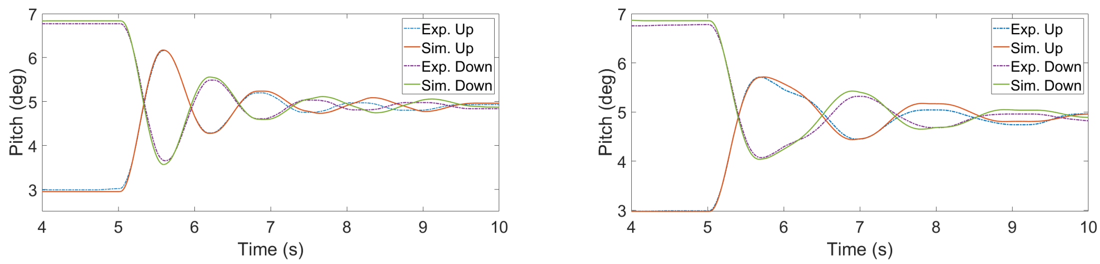

(a) Experimental and numerical results of decay tests for the case of WEC only

(b) Experimental and numerical results of decay tests for the case of WEC with bottom box

Figure 20. Experimental and numerical decay tests comparison at two different starting positions. The numerical model inputs a drag coefficient $Cd = 2$ and a constant moment due to bearings friction $Mfb = 0.4Nm$.

4.2. Regular waves simulations

The same version of the numerical model (V8, defined in Table 1) is now used to simulate free motion of WEC in regular waves, two examples are given in Figure 21. Figure 21a corresponds to the setup of WEC only, and in the case of this setup, the numerical model predicts with good agreement the displacement of the WEC from rest position that was observed in the wave basin. Figure 21b shows an experiment corresponding to one of the longest waves for the case where the WEC includes the fixed substructure, with a target wave period of 2s. In this case it was necessary to include an external linear damping moment to get a good match with measured data. The inclusion of linear damping moment was needed for wave periods longer than 1.4s in the case of WEC with bottom box, that is where a positive interaction between the two bodies was observed and predicted by potential theory. The value of the linear damping coefficient was selected based on the experimental data.

Preprints (www.preprints.org) | NOT PEER-REVIEWED | Posted: 9 January 2019 doi:10.20944/preprints201901.0078.v1

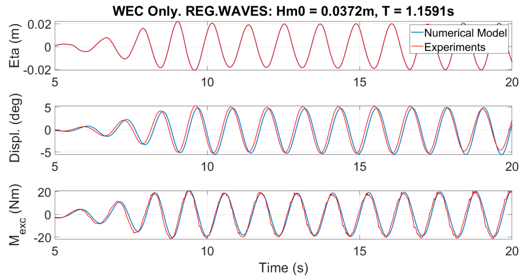

(a) Free motion of WEC in regular waves. Numerical model V8 with $Cd = 2$ and $M_{fb} = 0.4Nm$

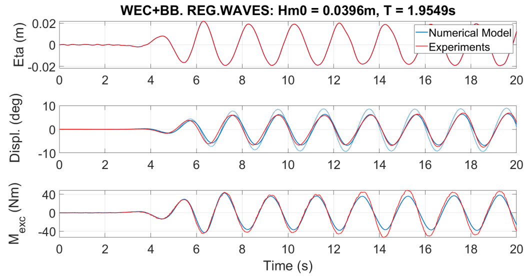

(b) Free motion of WEC+BB in regular waves. Numerical model V8 with $Cd = 2$, $M_{fb} = 0.4Nm$. Dotted blue: $C_{LinDamp} = 0$; solid blue: $C_{LinDamp} = 35$

Figure 21. Response Amplitude Operators for the WEC setup (left) and WEC+Bottom box setup (right). Solid blue line is RAO calculated with potential theory, blue dots are results from numerical model

To summarize the results of free motion in regular waves for both wave basin setups, (with and without bottom box), the response amplitude operators corresponding to each regular wave tested are included in Figure 22.

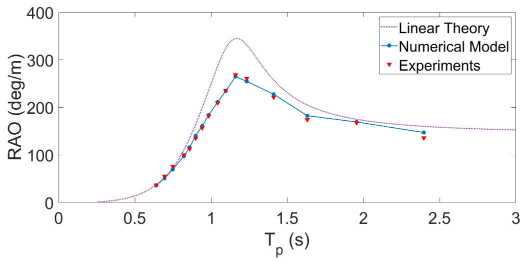

(a) Response Amplitude Operator for WEC only. Numerical model uses $Cd = 2$ and $M_{fb} = 0.4Nm$

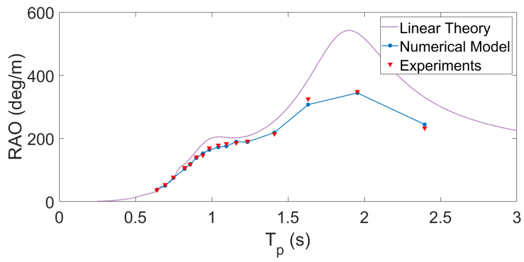

(b) Response Amplitude Operator for WEC with bottom box, $Cd = 2$, $M_{fb} = 0.4Nm$ and $C_{LinDamp} = 35$ for T=2s and T=2.5s and $C_{LinDamp} = 15$ for T=1.4s and T=1.6s

Figure 22. Response Amplitude Operators for the WEC setup (left) and WEC+Bottom box setup (right). Solid blue line is RAO calculated with potential theory, blue dots are results from numerical model

The phase shift obtained in the motion, can be due to experimental offsets. The waves causing the free motion of the body might have an offset relative to the waves measured during undisturbed wave experiments, which are the ones used as input to the numerical model.

4.3. Wave steepness

For the setup of WEC and bottom box, and for a target period of 1s, 5 different waves with different steepness were tested in the laboratory. However, neither radiation experiments nor excitation tests were done, so only the pitch motion can be compared with experimental data.

The numerical model shows that to accurately simulate the motion of the WEC for waves with steepness higher than $H/\lambda = 0.05$, the drag coefficient used to compute quadratic drag load needs to be reduced to $C_d = 1$, see Figure 23.

Preprints (www.preprints.org) | NOT PEER-REVIEWED | Posted: 9 January 2019 doi:10.20944/preprints201901.0078.v1

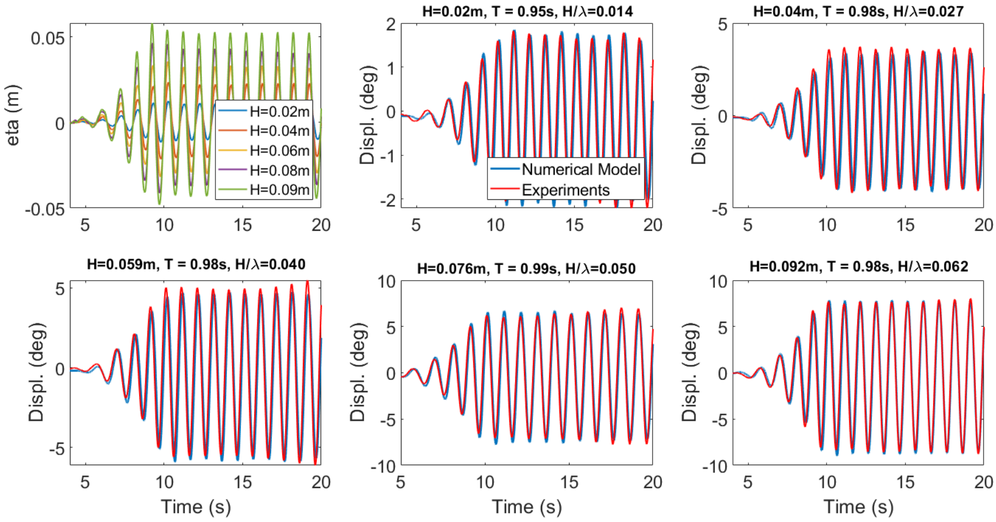

Figure 23. Modelling regular waves with different values of steepness. For waves with steepness values λ greater than 0.05, $C_d = 1$, for the other waves,$C_d = 2$. In the figure, H stands for wave height and T for wave period.

5. Discussion

A strong interaction between WEC and substructure was observed during experiments, with the surrounding fixed body making the WEC to operate with larger motions for the long waves. The hydrodynamic numerical model chosen to simulate the experiments computes the instantaneous wetted surface of the body, instantaneous water surface elevation with extrapolation of the wave kinematics above the mean water surface and an approximated quadratic drag load. The model also accounts for friction effects from the bearings measured in the laboratory. This version of the model is computationally effective and provides a close match to experimental data for both the pitch motion of the WEC and the wave excitation moment, provided the WEC is alone in the wave basin. However, when the fixed substructure is in place, the model overestimates the body motion for long waves, and it is needed to add a linear damping moment in order to get a good agreement with measured data. For this multi-body setup, the wave excitation moment differs more from the experimental wave excitation than in the case of WEC only.

Linear theory predicts the way that the WEC and the substructure are going to interact in, but overestimates the motion. The wave frequencies at which linear wave theory calculates a positive interaction between the two bodies (i.e. where the motion is increased due to the proximity of the second body), are the same wave frequencies at which an additional damping motion is required. Resonance of the water surface elevation under certain incident wave conditions may happen when bodies are closely spaced, this gap resonance magnifies the forces acting on the bodies and it is needed to include extra damping due to viscous effects to absorb this resonant energy. To improve the agreement between potential theory and experimental data, some methods, like the addition of flexible lids on the free surface inside the gaps have been studied [23]. To choose the damping paramenter to implement this lid in WAMIT, it is still necessary to count with experimental data. In addition, these flexible lids may affect the excitation, added mass, and radiation damping coefficients, so excitation and radiation experiments would also be needed to confirm these values. Studies of gap resonances have been investigated in other studies, mainly for cases of FLNG side-by-side offloading activities, highlighting the dominating linear behaviour of the system for the scaled geometries tested, and establishing a method to scale linear viscous damping for different gap width [24].

A complete validation of the model with experimental data is not achievable since some important experiments were not performed, like radiation tests, decay tests with different starting points, or

Preprints (www.preprints.org) | NOT PEER-REVIEWED | Posted: 9 January 2019 doi:10.20944/preprints201901.0078.v1

different free motion in waves for waves with different steepness values for both setups. Measurements of the water surface elevation in the gap are also crucial to determine gap resonances. Other experimental campaigns have been completed, including all these experiments, and some others like forced motions of the fixed platforms in 6 degrees of freedom. Wave gauges have also been located in the gaps of the system, so the wave behaviour can also be analysed in order to define the resonant effects and estimate the viscous linear damping load needed. Experiments with control strategies have also been done in order to validate power performance. Data analysis of these experiments has not been done yet, but once is completed, further validation/modifications of the numerical model will be done.

The multi-body single degree of freedom model presented in this paper is a starting point for a more complex one. The full scale device, complexity will increase, as it will consist of a semisubmersible platform moving as a rigid body in 6 degrees of freedom and 4 WECs, each one moving independently in pitch relative to the platform, with non-linear forces from power-take-off and mooring system. The dynamics of the WECs will have a high impact on the platform and, obviously, on the device's performance and power production. Before increasing the complexity of the model to this extent, it is needed a better understanding of the multi-body interactions of the single degree of freedom one in order.

6. Conclusions

FPP's experimental testing campaigns aim to generate high quality data for validation of numerical models. This paper presents the single degree of freedom numerical model development and the results from modelling experiments. A good match can be obtained when the WEC is tested alone, but when it has a fixed substructure around it, extra damping is required in the numerical model when simulating long waves. Experimental data has been key to building and calibrating the numerical model, however due to the limited time in the laboratory and the different objectives set for the experimental campaign, not all of the experiments needed were performed. Despite of this, the results achieved serve as a preliminary action towards FPP's code validation and further experiments have been performed or planned based on the experience gained during this testing phase.

Linear wave theory assumes small amplitudes of motion for the body. This assumption doesn't apply to FPP's WEC, since the angle of rotation changes and modifies the underbody within a short time lapse, being necessary to account for non-linear hydrostatic stiffness and excitation forces. Non-linear moments, like quadratic drag, have an important effect on the simulations providing good agreement for some cases. However, when the WEC interacts with another body in close proximity, adding quadratic drag is not enough and the motion of the WEC is still overpredicted. Quadratic drag coefficients are available in literature for some simple geometries, but there is no references for non-conventional geometries and complex configurations like the multibody setup presented in this study.

Acknowledgments: The research leading to these results has received funding from the European Union's Horizon 2020 research and innovation programme under the Marie Skodowska-Curie grant agreement No 675659 (ITN-EID ICONN Project).

References

1. http://floatingpowerplant.com/
2. Hamedni, B., Mathieu, C., Bittencourt-Ferreira, C.: Generic WEC System Breakdown. D5.1 of SDWED project. DNV-GL, Aalborg University (2014). https://www.sdwed.civil.aau.dk/digitalAssets/97/97538_d5.1.pdf
3. Weber, J.: WEC technology readiness and performance matrix—finding the best research technology development trajectory. In: 4th International Conference on Ocean Energy, Dublin (2012)
4. OES Task 10: Wave energy converters modelling verification and validation. https://bit.ly/2zv0ebb
5. Wendt, F. F., Yu, Y-H., Nielsen, K., Ruehl, K., Bunnik, T., Touzon, I., ... Hoffman, J. (2017). International Energy Agency Ocean Energy Systems Task 10 Wave Energy Converter Modeling Verification and Validation.

 doi:10.20944/preprints201901.0078.v1

In 12th EWTEC - Proceedings of the 12th European Wave and Tidal Energy Conference: 27th Aug -1st Sept 2017, Cork, Ireland [1197] Technical Committee of the European Wave and Tidal Energy Conference. European Wave and Tidal Energy Conference Series, No. 2017, Vol. 12

6. https://www.wamit.com/
7. Bellew S., Yde A., and Verelst D.R. Application of the aero-hydro-elastic model hawc2-wamit, to offshore data from floating power plants hybrid wind and wave energy test platform p37. In *5th International Conference on Ocean Energy (ICOE)*, 2014.
8. A. Yde, J. Larsen, A.M. Hansen, M. Fernandez, and S. Bellew. Comparison of simulations and offshore measurement data of a combined floating wind and wave energy demonstration platform. *Journal of Ocean and Wind Energy*, 2(3):129–137, 2015.
9. K. Ruehl, C. Michelen, Y.-H. Yu, and M. Lawson, "Update on WEC-Sim Validation Testing and Code Development," in Proceedings of the 4th Marine Energy Technology Symposium, METS 2016, DC, 2016.
10. Combourieu, Adrien and Lawson, Michael and Babarit, Aurélien and Ruehl, Kelley and Roy, André and Costello, Ronan and Weywada, Pauline Laporte and Bailey, Helen, "WEC 3 : Wave Energy Converter Code Comparison Project Preprint", Proceedings of the 11th European Wave and Tidal Energy Conference. 2015, Nantes, France
11. K. Ruehl, C. Michelen, B. Bosma, and Y.-H. Yu, "WEC-Sim Phase 1 Validation Testing – Numerical Modeling of Experiments," in Proceedings of the 35th International Conference on Ocean, Offshore and Arctic Engineering, OMAE 2016, Busan, South Korea, 2016
12. Kramer, M. WEC experiments and the equations of motion 2017 Maynooth University Wave Energy Workshop.
13. Le Mehaute, B. An introduction to Hydrodynamics and Water Waves; Springer Science & Business Media: New York, NY, USA, 1976.
14. Heras, P, Thomas, S and Kramer, MM 2017, Validation of Hydrodynamic Numerical Model of a Pitching Wave Energy Converter. In 12th EWTEC - Proceedings of the 12th European Wave and Tidal Energy Conference. 2017, Cork, Ireland.
15. https://en.wikipedia.org/wiki/Rotation_matrix, last accessed in December 2018.
16. Griet De Backer. *Hydrodynamic Design Optimization of Wave Energy Converters Consisting of Heaving Point Absorbers*. PhD thesis, Ghent University, 2009.
17. Retes, M.P., Mérigaud A., Gilloteaux J.C., and Ringwood, J. Nonlinear Froude-Krylov force modelling for two heaving wave energy point absorbers. In 11th EWTEC - Proceedings of the 11th European Wave and Tidal Energy Conference. 2015, Nantes, France.
18. Falnes, J. Ocean waves and oscillating systems: linear interactions including wave-energy extraction. Cambridge University Press, 2002.
19. Housseine C, Monroy C, de Hauteclocque G. Stochastic Linearization of the Morison Equation Applied to an Offshore Wind Turbine. ASME. International Conference on Offshore Mechanics and Arctic Engineering, Volume 9: Ocean Renewable Energy ():V009T09A040. doi:10.1115/OMAE2015-41301.
20. http://mathworld.wolfram.com/TriangleArea.html, last accessed in December 2018.
21. https://math.stackexchange.com/questions/2041099/angle-between-vectors-given-cross-and-dot-product, last accessed in December 2018
22. Hoerner, S.F., 1965. Fluid-Dynamic Drag, Hoerner Fluid Dynamics, Bricktown New Jersey, 1965
23. Newman, J.N., 2001. Wave effects on multiple bodies. In: Kashiwagi, M. (Ed.), Hydrodynamics in Ship and Ocean Engineering. RIAM, Kyushu University, Japan, pp.3-26.
24. Zhao, Wenhua and Taylor, Paul H. and Wolgamot, Hugh A. and Taylor, Rodney Eatock. Linear viscous damping in random wave excited gap resonance at laboratory scale — NewWave analysis and reciprocity. Journal of Fluids and Structures, vol. 80, pp.59-76. July, 2018.